Journal of Alloys and Compounds 509 (2011) 5349–5355

Contents lists available at ScienceDirect

Journal of Alloys and Compounds

journal homepage: www.elsevier.com/locate/jallcom

Structural, optical and EPR studies on ZnO:Cu nanopowders prepared via low temperature solution combustion synthesis

A. Jagannatha Reddy[a], M.K. Kokila[b], H. Nagabhushana[c,*], R.P.S. Chakradhar[d,*], C. Shivakumara[e], J.L. Rao[f], B.M. Nagabhushana[g]

[a] Department of Physics, M. S. Ramaiah Institute of Technology, Bangalore 560 054, India
[b] Department of Physics, Bangalore University, Bangalore 560 056, India
[c] Advanced Materials Research Laboratory, Tumkur University, Tumkur 572 103, India
[d] Central Glass and Ceramic Research Institute (CSIR), Kolkata 700 032, India
[e] Solid State and Structural Chemistry Unit, Indian Institute of Science, Bangalore 560 012, India
[f] Department of Physics, S.V. University, Tirupathi 517 502, India
[g] Department of Chemistry, M. S. Ramaiah Institute of Technology, Bangalore 560 054, India

ARTICLE INFO

Article history:
Received 12 November 2010
Received in revised form 4 February 2011
Accepted 7 February 2011
Available online 12 February 2011

Keywords:
ZnO
Nanopowder
XRD
SEM
TEM
UV–Vis
Photoluminescence
EPR

ABSTRACT

Cu (0.1 mol%) doped ZnO nanopowders have been successfully synthesized by a wet chemical method at a relatively low temperature (300 °C). Powder X-ray diffraction (PXRD) analysis, scanning electron microscopy (SEM), Transmission electron microscopy (TEM), Fourier transformed infrared (FTIR) spectroscopy, UV–Visible spectroscopy, Photoluminescence (PL) and Electron Paramagnetic Resonance (EPR) measurements were used for characterization. PXRD results confirm that the nanopowders exhibit hexagonal wurtzite structure of ZnO without any secondary phase. The particle size of as-formed product has been calculated by Williamson–Hall (W–H) plots and Scherrer's formula is found to be in the range of ~40 nm. TEM image confirms the nano size crystalline nature of Cu doped ZnO. SEM micrographs of undoped and Cu doped ZnO show highly porous with large voids. UV–Vis spectrum showed a red shift in the absorption edge in Cu doped ZnO. PL spectra show prominent peaks corresponding to near band edge UV emission and defect related green emission in the visible region at room temperature and their possible mechanisms have been discussed. The EPR spectrum exhibits a broad resonance signal at $g \sim 2.049$, and two narrow resonances one at $g \sim 1.990$ and other at $g \sim 1.950$. The broad resonance signal at $g \sim 2.049$ is a characteristic of Cu^{2+} ion whereas the signal at $g \sim 1.990$ and $g \sim 1.950$ can be attributed to ionized oxygen vacancies and shallow donors respectively. The spin concentration (N) and paramagnetic susceptibility (χ) have been evaluated and discussed.

1. Introduction

Zinc oxide (ZnO) is a direct wide band gap (3.37 eV) II–VI semiconductor, having high exciton binding energy (60 meV) and has stable wurtzite structure with lattice spacing $a = 0.325$ nm and $c = 0.521$ nm. Doping is a widely used method to improve electrical, optical, and mechanical properties of semiconductor compounds, facilitating the construction of many electronic and optoelectronic devices. Doped ZnO is of considerable significance for its use in industry as information storage materials, fluorescent lamps, control panel displays, plasma display panels, field effect transistor [1–5] antireflection coatings, transparent electrodes in solar cells, ultraviolet (UV) light emitters, diode lasers, varistors, piezoelectric devices, surface acoustic wave propagator [6,7], anti bacterial agent [8], photonic material [9] and for gas sensing [10]. Theoretical and experimental studies showed that ZnO doped with appropriate transition metals (TM) are diluted magnetic semiconductors (DMS) [11] which attracted a lot of interest due to their potential applications in spintronics [12].

Different physical or chemical synthetic approaches have been developed to produce nano-sized ZnO particles including thermal decomposition, thermolysis [13], chemical vapor deposition, sol–gel [14,15], spray pyrolysis, precipitation [16–20] vapor phase oxidation [21], thermal vapor transport, condensation [22] and hydrothermal [23,24]. Generally, these preparation methods involve complex procedures, sophisticated equipment and rigorous experimental conditions. Most of these techniques require high temperatures and long processing time. Indeed, there is great demand for economically viable synthesis techniques. Solution

* Corresponding author. Present address: Scientist, CSIR-NAL, Bangalore 560 017, India.
E-mail addresses: drmkkokila@gmail.com (M.K. Kokila), bhushanvl@rediffmail.com (H. Nagabhushana), sreechakra72@yahoo.com (R.P.S. Chakradhar).

0925-8388/$ – see front matter © 2011 Elsevier B.V. All rights reserved.
doi:10.1016/j.jallcom.2011.02.043

combustion synthesis (SCS) is emerging as a promising technique for the preparation of nanopowders. This process is simple, fast and economic, does not require high-temperature furnaces and complicated set-ups. It can be used for the preparation of all kinds of oxides [25].

In the present study, SCS is used to prepare the Cu doped ZnO nano particles. Typically SCS involves a self-sustained reaction in solutions of metal nitrates and different fuels. The following features of SCS contribute to the unique properties of the synthesized products. First, the initial reaction media existence in the liquid state (e.g. aqueous solution) allows mixing of the reactants at a molecular level, thus permitting precise and uniform formulation of the desired composition on the nanoscale. Second, the high reaction temperatures (>1000 °C) ensure high product purity and crystallinity. This feature allows one to skip an additional step, i.e., high temperature product calcinations, which typically follow the conventional sol–gel and solid state approach, to achieve the desired phase composition. Third, the short process duration and formation of various gases during SCS inhibit particle size growth and favor synthesis of nanosized powders with a high specific surface area.

2. Experimental

2.1. Synthesis

The stoichimetric quantities of analytical grade $Zn(NO_3)_2$, $Cu(NO_3)_2$ and fuel $C_2H_6N_4O_2$ (oxalyl dihydrazide, ODH) are dissolved in minimum quantity of double distilled water. These quantities determine the total oxidizing (O) and reduction (F) valencies of the components so that the equivalence ratio ψ is unity (i.e., $O/F = 1$) and the energy released by the combustion is at a maximum. The Petri dish containing this solution was placed in a pre-heated muffle furnace set at 300 °C. The solution boiled resulting in a transparent gel. The gel then formed white foam, which expanded to fill the vessel. Shortly thereafter, the reaction was initiated somewhere in the interior and a flame appeared on the surface of the foam and proceeded rapidly throughout the entire volume, leaving a white powder with an extremely porous structure. The energy released from the reaction can produce temperatures in excess of 1000 °C. The reaction is self-propagating and is able to sustain this high temperature long enough, from 1 to 5 s typically, to form the desired product. The entire combustion process was over in about 5 min. The detailed flow chart of combustion synthesis is illustrated in Fig. 1.

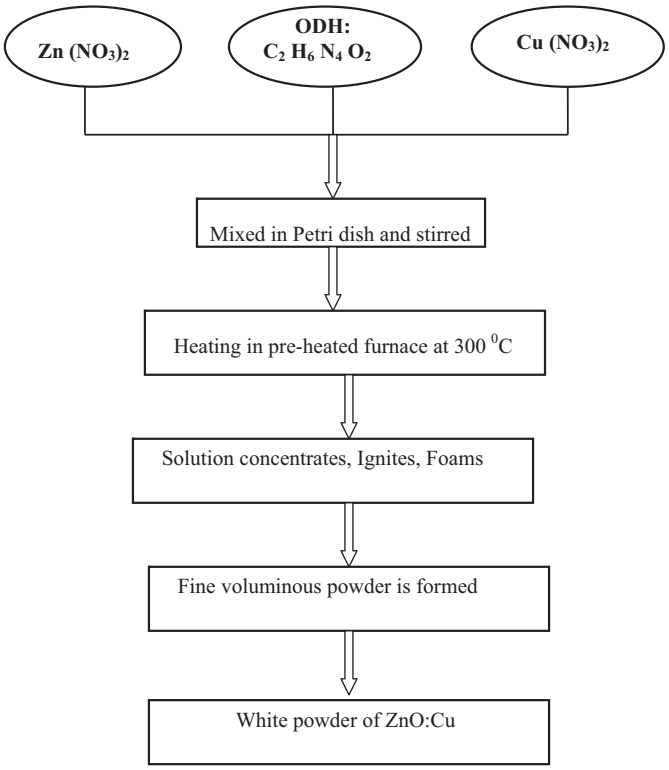

Fig. 1. Flow chart for the combustion synthesis of ZnO:Cu nanopowders.

2.2. Instruments

The powder X-ray diffraction studies were carried out using Phillips X-ray diffractometer (model PW 3710) with Cu Kα radiation (λ = 1.5405 Å). The surface morphology of the samples was examined using Scanning electron microscopy (SEM) (JEOL JSM 840A). Transmission Electron Microscopy (TEM) analysis was performed on a Hitachi H-8100 (accelerating voltage up to 200 kV, LaB_6 filament) (Kevex Sigma TM Quasar, USA). The UV-Vis spectrum was recorded on a UV-3101 Shimadzu Visible spectrophotometer. The photoluminescence (PL) studies were carried out using a Perkin–Elmer LS-55 luminescence spectrophotometer equipped with Xe lamp (excitation wavelength 250 nm). The EPR spectra were recorded at room temperature using a JEOL-FE-1X EPR spectrometer operating in the X-band frequency (≈9.205 GHz) with a field modulation frequency of 100 kHz. The magnetic field was scanned from 0 to 500 mT and the microwave power used was 10 mW. A powdered specimen of 100 mg was taken in a quartz tube for EPR measurements.

3. Results and discussion

3.1. Powder X-ray diffraction (PXRD)

Fig. 2 shows the PXRD profiles of undoped and Cu doped ZnO nanopowders. All diffraction peaks corresponding to (1 0 0), (0 0 2), (1 0 1), (1 0 2), (1 1 0), (1 0 3), (1 1 2) planes were in agreement with typical hexagonal wurtzite structure of pure ZnO. No additional peaks corresponding to any secondary or impurity phase were observed which confirms the phase purity of the sample. Quantitative information concerning the preferential crystallite orientation was obtained from the texture coefficient TC($h\,k\,l$) defined as

$$TC_{hkl} = \frac{\left(I_{hkl}/I_o\right)}{\left(\sum I_{hkl}/I_o\right)} \times 100\% \qquad (1)$$

where $I(h\,k\,l)$ is the measured relative intensity of a plane ($h\,k\,l$), and $I_0(h\,k\,l)$ is the standard intensity of the plane taken from the JCPDS data. The value TC($h\,k\,l$) = 1 represents randomly oriented crystallite, while higher values indicate the abundance of grains oriented in a given ($h\,k\,l$) direction. From the texture coefficient values obtained, (1 0 0), (0 0 2), and (1 0 1) planes are the preferential crystallite orientation for the nano-sized ZnO particles fabricated in this study. The average crystallite size (D) was estimated from the Debye–Scherrer's equation

$$D = \frac{0.9\lambda}{\beta \cos\,\theta} \qquad (2)$$

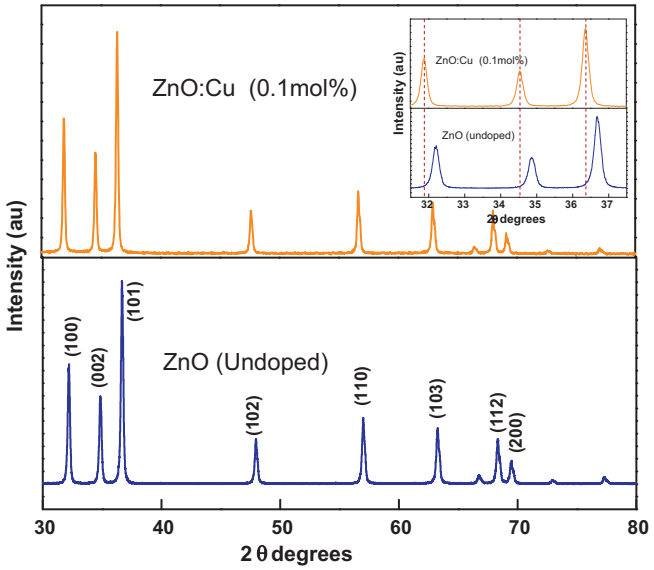

Fig. 2. PXRD patterns of undoped and Cu doped ZnO nanopowders.

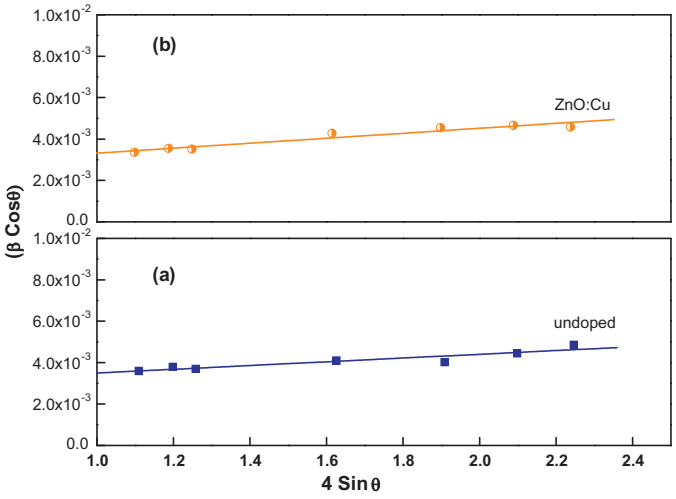

Fig. 3. W–H plots of (a) undoped ZnO and (b) Cu doped ZnO nanopowders.

where λ represents the wavelength of the X-ray radiation, β is the full width at half maximum (FWHM) of diffraction peak (in rad) and θ is the scattering angle. The crystallite size calculated for Cu doped sample (37 nm) was found to be less compared to undoped ZnO (40 nm).

A small shift in the position of main peaks (Inset of Fig. 2) to the lower side of 2θ values and broadening of XRD peaks are observed for Cu doped sample. A peak shift in XRD profiles arises due to the presence of micro strains in the sample [26] but the line broadening might also be observed. It is commonly accepted that XRD line broadening may be the result of pure size, or micro strain, or both size and micro strain broadening. Williamson and Hall (W–H) have suggested a method [27] combining the domain size and lattice micro strain effects on line broadening, when both are operative. The W–H approach considers the case when the domain effect and lattice deformation are both simultaneously operative and their combined effects give the final line broadening FWHM (β), which is the sum of β (grain size) and β (lattice distortion). This relation assumes a negligibly small instrumental contribution compared to the sample-dependent broadening. W–H equation may be expressed in the form

$$\beta \cos\theta = \frac{k\lambda}{D} + 4\varepsilon \sin\theta \quad (3)$$

where ε is the strain associated with the nanoparticles. Eq. (3) represents a straight line between $4\sin\theta$ (X-axis) and $\beta\cos\theta$ (Y-axis). The slope of line gives the strain (ε) and intercept ($k\lambda/D$) of this line

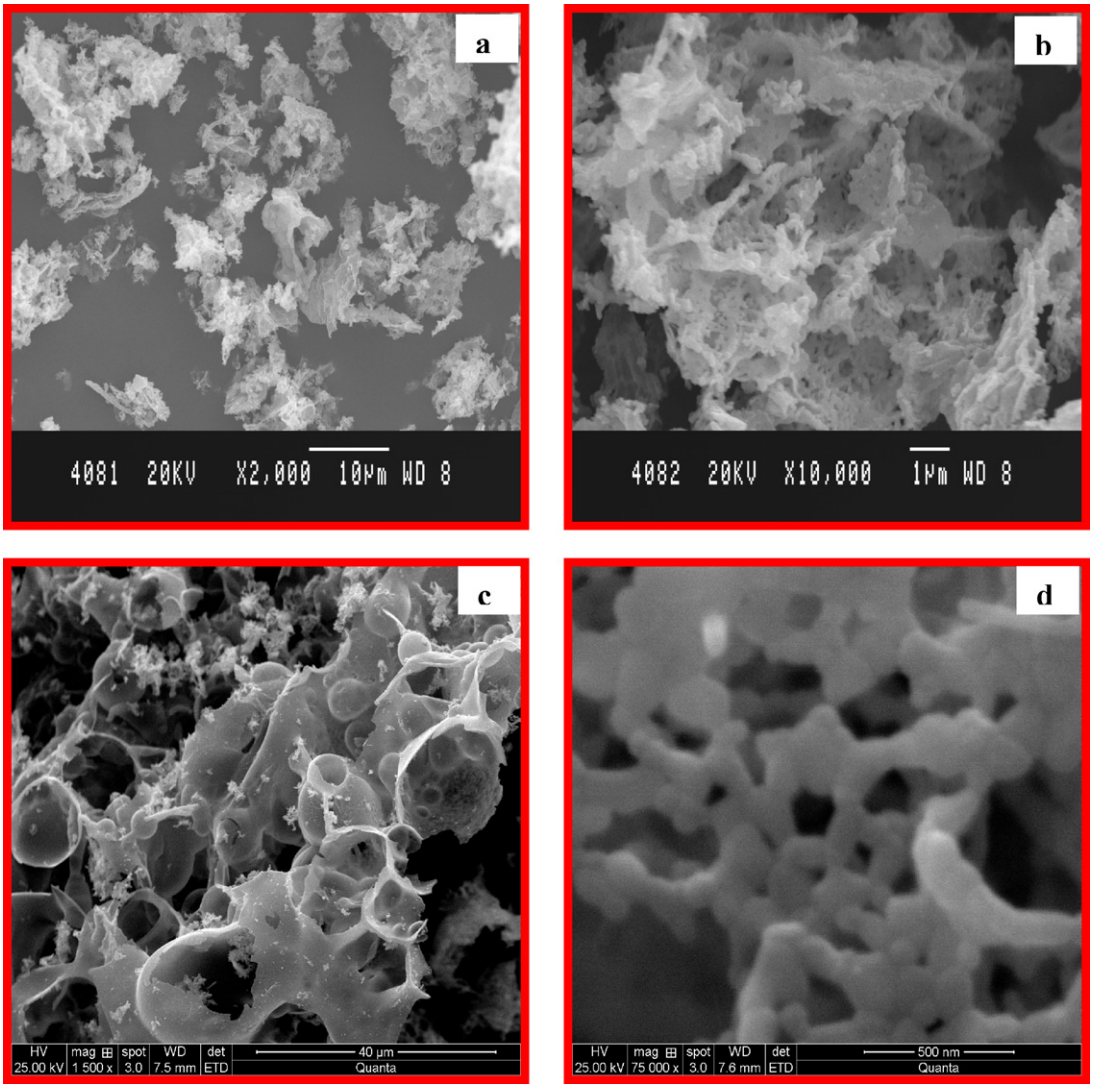

Fig. 4. SEM images of undoped (a and b) and Cu doped (c and d) ZnO nanopowders.

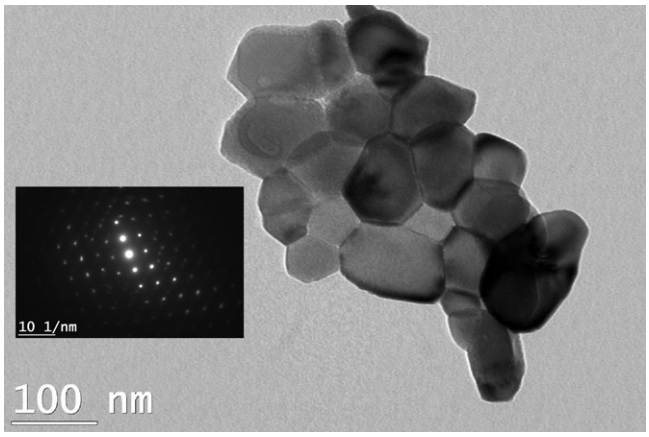

Fig. 5. TEM image of Cu doped ZnO nanopowder (selected area electron diffraction (SAED) patterns).

on *Y*-axis gives grain size (*D*). Fig. 3 shows W–H plots of (a) undoped and (b) Cu doped ZnO samples. The XRD data of all the (*h k l*) planes were used to construct the W–H plots. It is observed that the strain for Cu doped sample (1.212×10^{-3}) is greater than that of undoped ZnO (0.906×10^{-3}). This increase in strain causes the broadening and shift in XRD peaks in Cu doped sample. The crystallite size calculated from the *Y*-intercept in W–H plots for Cu doped sample (40 nm) was found to be less compared to undoped ZnO (42 nm). These values are in good agreement with that obtained from Debye–Scherrer's equation.

3.2. Scanning and transmission electron microscopy (SEM and TEM)

The surface morphology of undoped and Cu doped ZnO samples is studied using SEM (Fig. 4). It can be clearly observed from low resolution SEM images that, the powders show many agglomerates with an irregular morphology. In case of undoped ZnO, particles are connected to each other to make large network systems with irregular pore sizes and shapes (Fig. 4a and b). In Cu doped ZnO, the powder shows honeycomb structure with broken type of hollow shells formed by the escaping gases during combustion (Fig. 4c). This type of porous network with lot of voids is typical of combustion synthesized powders due to escaping gases. These porous powders are highly friable which facilitates easy grinding to obtain finer particles. Higher magnification SEM micrograph shows the presence of several small particles within the grains (Fig. 4d). It can be observed that the crystallites have no uniform shape. This is believed to be related to the non-uniform distribution of temperature and mass flow in the combustion flame. Fig. 5 depicts the TEM image of Cu doped ZnO particles which are quasi-hexagonal in shape having average size in the range of 40–50 nm. This was also confirmed by Debye–Scherrer's equation and W–H plots. Hence, it can be concluded that the obtained particles are not polycrystalline in nature. Further, the same results are confirmed by selected area electron diffraction (SAED) patterns shown in Fig. 5.

3.3. Fourier transformed infrared spectroscopy (FTIR)

The purity and molecular structure of product were analyzed by the FTIR spectroscopy. Fig. 6 shows the FTIR spectrum of the undoped and Cu doped ZnO nanocrystalline powder which was acquired in the range of 400–4000 cm^{-1}. The two peaks at ~3428 and 1590 cm^{-1} are attributed to O–H stretching vibration and H–O–H bending vibration, which are assigned to small amount of H_2O existing in the nanocrystalline ZnO. The peak at 420 cm^{-1} is ascribed to Zn–O stretching vibration. No other impurity peaks related to other groups are observed which shows the purity of the sample.

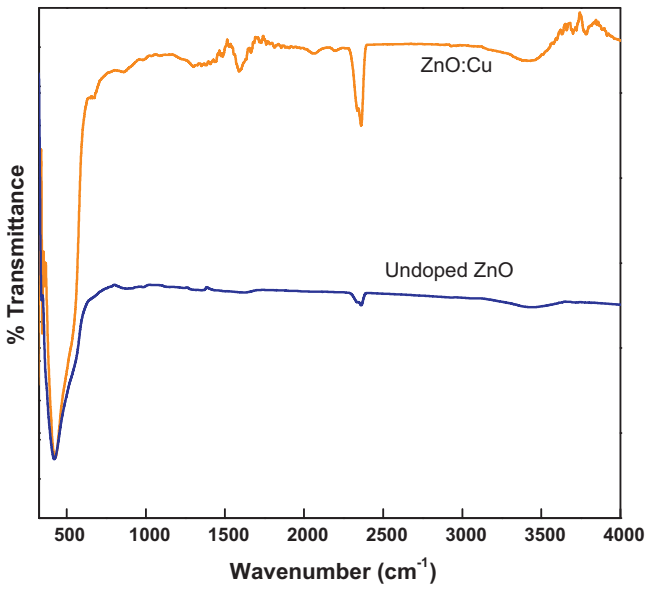

Fig. 6. FTIR spectra of undoped and Cu doped ZnO nanopowders.

3.4. UV-Visible absorption spectrum

UV–Vis spectroscopic measurements were carried out at room temperature to study the effect of Cu doping on ZnO in the range 300–800 nm. The UV–Vis absorption spectrum of undoped and Cu doped ZnO sample is shown in Fig. 7. A red shift in the absorption edge is observed in Cu doped ZnO which may be related to formation of shallow levels inside the band gap due to doping. The optical energy band gap E_g of samples was estimated using the Tauc relation [28]

$$(ah\upsilon) \sim (h\upsilon - E_g)^{1/2} \quad (4)$$

where $h\upsilon$ is the photon energy and α is the optical absorption coefficient near the fundamental absorption edge. The absorption coefficients were calculated from the optical absorption spectra. The optical band gap of ZnO is obtained by plotting $(\alpha h\upsilon)^2$ versus $(h\upsilon)$ in the high-absorption range followed by extrapolating the

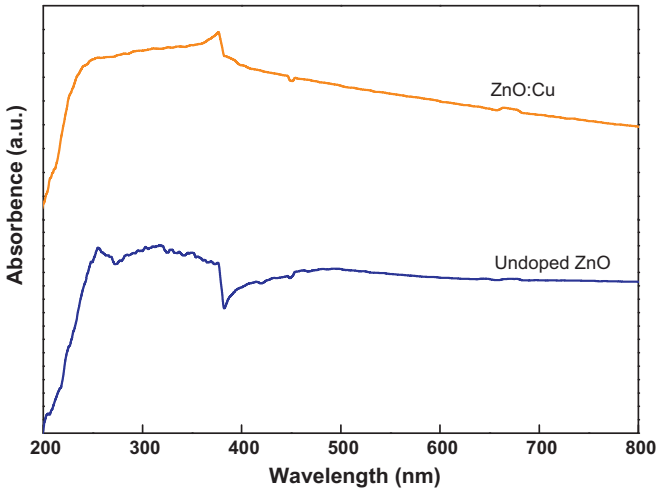

Fig. 7. UV–Vis spectra of undoped and Cu doped ZnO nanopowders.

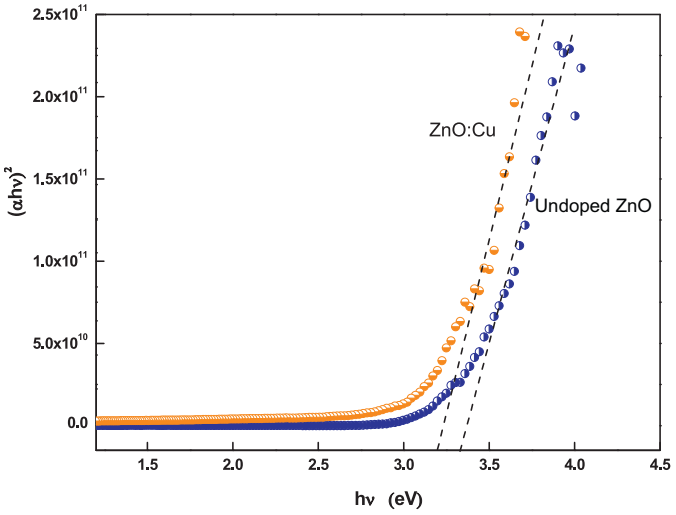

Fig. 8. Band gap of undoped and Cu doped ZnO nanopowders.

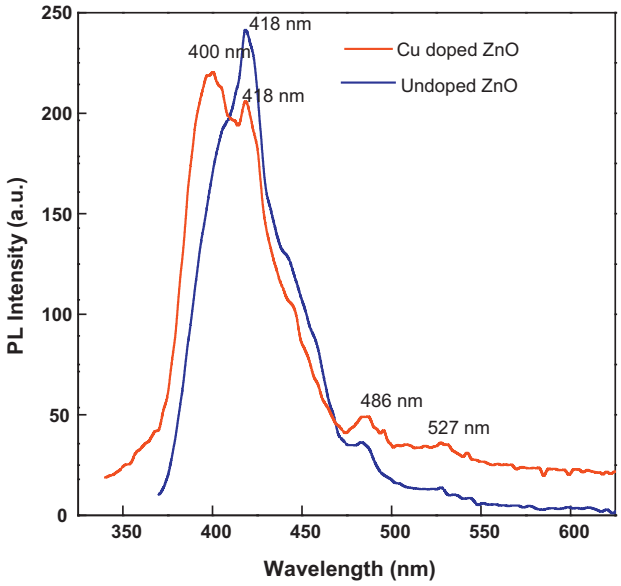

Fig. 9. PL emission spectrum of undoped and Cu doped ZnO nanopowders (λ_{exi} = 325 nm).

linear region of the plots to $(\alpha h\upsilon)^2 = 0$ (Fig. 8). From the figure it is seen that the Cu doped ZnO sample has an optical energy band gap of 3.04 eV that is lower than that of the undoped ZnO (3.28 eV). Similar red shift in energy band gap of transition-metal doped II–VI semiconductors was reported by Diouri et al. [29,30] which was attributed to the p–d spin-exchange interactions between the band electrons and the localized d electrons of transition-metal ion substituting the cation. Elilarassi et al. [31] observed a red shift in the band gap in Cu doped ZnO nanoparticles synthesized by solid state reaction method. Ferhat et al. [32] also found a reduction of band gap in Cu doped ZnO. The analysis of the partial density of states reveals that narrowing of ZnO band gap is due principally to the strong p–d mixing of O and Cu. The mechanism behind the s–d and p–d exchange interactions was theoretically explained by Bylsma et al. [33] using the second-order perturbation theory which was attributed to the band gap shrinkage. The red shift in band gap of combustion derived Cu doped sample confirms the uniform substitution of Cu for Zn ions in the lattice.

3.5. Photoluminescence (PL) studies

Fig. 9 shows the typical room temperature photoluminescence spectrum of as-prepared undoped and Cu doped ZnO nanopowders. In case of undoped ZnO, a high-intensity sharp peak at 418 nm in the violet-region was observed while low intensity peaks at 486 and 527 nm were observed in the blue–green and green region. However, the PL spectra of copper-doped ZnO samples consist of an additional peak in the ultra violet band centered at 400 nm. The ultraviolet-emission also known as near band edge emission (NBE) of the wide band gap ZnO is attributed to the exciton transition from the localized level below the conduction band to the valance band [34,35] while defect related visible emissions in ZnO nanomaterials may be ascribed to the intrinsic defects such as oxygen vacancies (V_o), Zinc vacancies (V_{Zn}), oxygen interstitials (O_i), Zinc interstitials (Zn_i) and oxygen antisites (O_{Zn}) [36,37]. The blue–green emission centered at 486 nm is due to a radiative transition of an electron from the deep donar level of Zn_i to an acceptor level of neutral V_{Zn} [38]. The green emission at 527 nm is attributed to radiative transition of an electron from the deep donor level of Zn_i to an acceptor level caused by singly ionized charged state of the defect V_{Zn}^- in ZnO [39–42] as illustrated in the energy level diagram (Fig. 10) representing the emission probabilities from respective luminescence centers. Cu-doping can effectively reduce the defects such as oxygen vacancies and zinc vacancies in ZnO nanocrystals [31,43,44]. Thus, in Cu doped ZnO sample, the intensity of defect related green emission decreased slightly with enhanced UV emis-

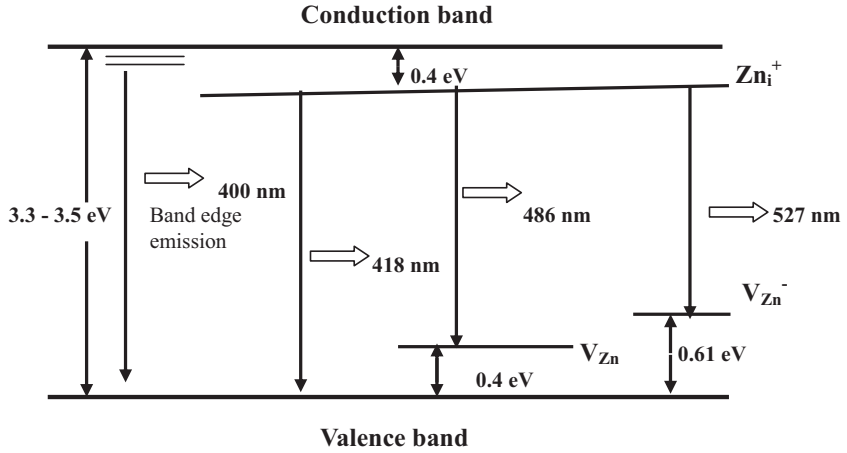

Fig. 10. Energy levels of defects present in the band gap of ZnO.

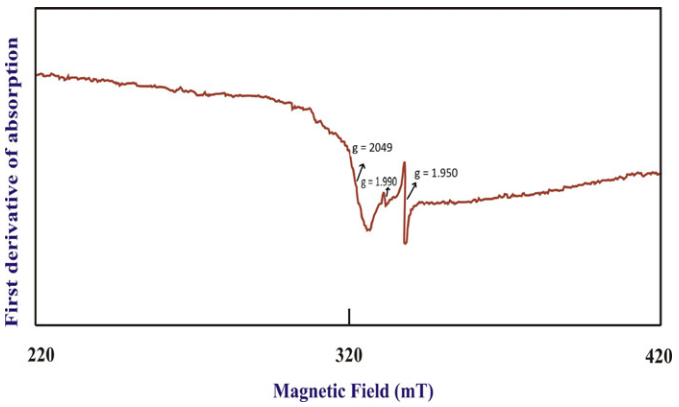

Fig. 11. EPR spectrum of Cu doped ZnO nanopowder.

sion. This strongly depicts that the concentration of the defects responsible for deep-level emissions could be reduced by Cu doping in ZnO and also it is possible to tune the UV emission.

3.6. Electron paramagnetic resonance (EPR) studies

Fig. 11 shows the EPR spectrum of Cu doped ZnO nanocrystalline powder recorded at room temperature. The EPR spectrum exhibits a broad resonance signal at $g \sim 2.049$, and two narrow resonances one at $g \sim 1.990$ and other at $g \sim 1.950$. The broad resonance signal at $g \sim 2.049$ is a characteristic of Cu^{2+} ion. It is evident from literature that, various behaviors of ZnO are due to the presence of native defects, such as oxygen vacancies and zinc vacancies. Most of the experimental investigations of oxygen vacancies in ZnO to date have relied on the EPR measurements. Many of these studies fall on two categories based on the *g*-factor: one set of reports associates oxygen vacancies with $g \sim 1.960$, the other with $g \sim 1.990$. There is overwhelming evidence that oxygen vacancies are actually associated with the $g \sim 1.990$ line. Therefore, EPR signal in the present study at $g \sim 1.990$ has been unambiguously assigned to singly ionized oxygen vacancies [45,46]. The resonance signal observed at $g \sim 1.950$ can be attributed to shallow donors and it shows slight anisotropy due to the wurtzite crystal structure. In general this signal will be observed in nano crystals with diameters larger than 20 nm, due to the random orientations of the nanocrystals and this signal is isotropic [47].

3.7. Calculation of spin concentration (N)

The number of Cu^{2+} ions participating in resonance can be calculated by comparing the area under the absorption curve with that of a standard ($CuSO_4{\cdot}5H_2O$ in this study) known concentration. Weil et al. [48] gave the following expression which includes the experimental parameters of both sample and standard.

$$N = \frac{A_x(Scan_x)^2 G_{std}(B_m)_{std}(g_{std})^2[S(S+1)]_{std}(P_{std})^{1/2}}{A_{std}(Scan_{std})^2 G_x(B_m)_x(g_{std})^2[S(S+1)]_x(P_x)^{1/2}}[std] \quad (5)$$

where *A* is the area under the absorption curve which can be obtained by double integrating the first derivative EPR absorption curve, *scan* is the magnetic field corresponding to unit length of the chart, *G* is the gain, B_m is the modulation field width, *g* is the *g* factor, *S* is the spin of the system in its ground state. *P* is the power of the microwave source. The subscripts '*x*' and '*std*' represent the corresponding quantities for Cu^{2+} in ZnO sample and the reference ($CuSO_4{\cdot}5H_2O$) respectively. The number of Cu^{2+} ions participating in resonance for $g = 2.049$ at room temperature is found to be 1.55×10^{22}.

3.8. Calculation of paramagnetic susceptibility (χ) from EPR data

The EPR data can be used to calculate the paramagnetic susceptibility of the sample using the formula [49]

$$\chi = \frac{Ng^2\beta^2 J(J+1)}{3k_B T} \quad (6)$$

where '*N*' is the number of spins per m^3, 'β' is the Bohr magneton, 'J' is the total angular momentum, 'k_B' is the Boltzmann constant and '*T*' is the absolute temperature. The number of spins '*N*' can be calculated by double integrating the first derivative EPR spectrum and $g = 2.049$ is taken from EPR data. The paramagnetic susceptibility at room temperature is found to be 3.96×10^{-3} emu/mol. We chose to determine the spin susceptibility from EPR, because this technique has several advantages over a static measurement, where a diamagnetic contribution must be subtracted.

4. Conclusions

Cu has been successfully incorporated into ZnO lattice by solution combustion method at much lower temperature. PXRD pattern shows that the nanopowders have typical hexagonal wurtzite structure with particle size in the range of ~40 nm. The characterization of the samples confirmed that Cu dopant substitute for Zn cation sites homogeneously. For undoped ZnO, the particles are connected to each other to make large network systems with irregular pore sizes and shapes whereas, in Cu doped ZnO, the powder shows honeycomb structure with broken type of hollow shells formed by the escaping gases during combustion. A red shift and narrowing of band gap in Cu doped ZnO is due principally to the strong p–d mixing of O and Cu and it confirms the incorporation of Cu into ZnO lattice. From PL study, slight decrease in the green emission and enhancement of UV emission in Cu doped ZnO might be due to the decrease in defects. The EPR spectrum exhibits a broad resonance signal at $g \sim 2.049$, and two narrow resonances one at $g \sim 1.990$ and other at $g \sim 1.950$. The broad resonance signal at $g \sim 2.049$ is a characteristic of Cu^{2+} ion whereas the signal at $g \sim 1.990$ and $g \sim 1.950$ can be attributed to ionized oxygen vacancies and shallow donors respectively. The number of spins participating in resonance and its paramagnetic susceptibility (χ) is found to be 1.55×10^{22} and 3.96×10^{-3} emu/mol respectively. We chose to determine the spin susceptibility from EPR, because this technique has several advantages over a static measurement, where a diamagnetic contribution must be subtracted.

Acknowledgements

The authors are thankful to Chemistry TEQIP Laboratory of M.S.R.I.T. Bangalore for providing facilities for preparation of materials. A. Jagannatha Reddy is grateful to the Principal and management of M.S.R.I.T. for continuous support and encouragement. One of the authors HN thanks Dr. S.C. Sharma, Vice Chancellor, Tumkur University, Tumkur for constant encouragement and support.

References

[1] X. Feng, J. Phys.: Condens. Matter 16 (2004) 4251.
[2] R. Renzt, H.J. Schulz, J. Phys. C: Solid State Phys. 16 (1983) 4917.
[3] N. Ohashi, N. Ebisawa, T. Sekiguchi, I. Sakaguchi, Y. Wada, T. Takenaka, H. Haneda, Appl. Phys. Lett. 86 (2005) 91902.
[4] C.R. Ronda, J. Lumin. 72 (1997) 49.
[5] K. Borgohain, S. Mahamuni, Semicond. Sci. Technol. 13 (1998) 1154.
[6] U. Ozgur, Ya. I. Alivov, C. Liu, A. Teke, M.A. Reshchikov, S. Dogan, V. Avrutin, S.J. Cho, H. Morko, J. Appl. Phys. 98 (2005) 041301.
[7] C.R. Gorla, N.W. Emanetoglu, S. Liang, W.E. Mayo, Y. Lu, M. Wraback, H. Shen, J. Appl. Phys. 85 (1999) 2595.
[8] L. Zhang, Y. Ding, M. Povey, D. York, Prog. Nat. Sci. 18 (2008) 939.

[9] J. Xie, H. Deng, Z.Q. Xu, Y. Li, J. Huang, J. Cryst. Growth 292 (2006) 227.
[10] C. Liewhiran, S. Phanichphant, Sensors 7 (2007) 650.
[11] R. Janisch, P. Gopal, N.A. Spaldin, J. Phys. Condens. Matter 17 (2005) 657.
[12] S.A. Wolf, D.D. Awschalom, R.A. Buhrman, J.M. Daughton, S. von Molnar, M.L. Roukes, A.Y. Chtchelkanova, D.M. Treger, Science 294 (2001) 1488.
[13] Masoud Salavati-Niasari, Fatemeh Davar, Afsaneh Khansari, J. Alloys Compd. 509 (2011) 61.
[14] Deyi Wang, Jian Zhoua, Guizhen Liua, J. Alloys Compd. 487 (2009) 545.
[15] Jinghai Yang, Lianhua Feia, Huilian Liua, Yang Liu, Ming Gaoa, Yongjun Zhanga, Lili Yanga, J. Alloys Compd. 509 (2011) 3672.
[16] Y. Yang, H. Chen, B. Zhao, X. Bao, J. Cryst. Growth 263 (2004) 447.
[17] M. Purica, E. Budianu, E. Rusu, M. Danila, R. Gavrila, Thin Solid Films 403 (2002) 485.
[18] J.H. Lee, K.H. Ko, B.O. Park, J. Cryst. Growth 247 (2003) 119.
[19] R. Ayouchi, D. Leinen, F. Martin, M. Gabas, E. Dalchiele, J.R. Ramos-Barrado, Thin Solid Films 426 (2003) 68.
[20] Z.M. Dang, L.Z. Fan, S.J. Zhao, C.W. Nan, Mater. Sci. Eng. B 99 (2003) 386.
[21] J.Q. Hu, Q. Li, N.B. Wong, C.S. Lee, S.T. Lee, Chem. Mater. 14 (2002) 1216.
[22] J.Y. Lao, J.Y. Huang, D.Z. Wang, Z.F. Ren, Nano Lett. 3 (2003) 235.
[23] R. Savu, R. Parra, E. Joanni, B. Jancar, S.A. Elizario, R. de Camargo, P.R. Bueno, J.A. Varela, E. Longo, M.A. Zaghate, J. Cryst. Growth 311 (2009) 4102.
[24] T. Al-Harbi, J. Alloys Compd. 509 (2011) 387.
[25] J.J. Kingsley, K.C. Patil, Mater. Lett. 6 (1988) 427.
[26] J. Pelleg, E. Elish, J. Vac. Sci. Technol. A20 (2002) 754.
[27] G.K. Williamson, W.H. Hall, Acta Metall. 1 (1953) 22–31.
[28] H. Nagabhushana, B.M. Nagabhushana, Madesh Kumar, H.B. Premkumar, C. Shivakumara, R.P.S. Chakradhar, Philos. Mag. 26 (2010) 3567.
[29] J. Diouri, J.P. Lascaray, M. El Amrani, Phys. Rev. B 31 (1985) 7995.
[30] Xue-Yong Li, Hong-Jian Lia, Ming Yuan, Zhi-Jun Wang, Zi-You Zhou, Ren-Bo Xu, J. Alloys Compd. 509 (2011) 3025.
[31] R. Elilarassi, G. Chandrasekaran, J. Mater. Sci.: Mater. Electron. 21 (2010) 1168.
[32] M. Ferhat, A. Zaoui, R. Ahuja, Appl. Phys. Lett. 94 (2009) 142502.
[33] R.B. Bylsma, W.M. Becker, J. Kossut, U. Debska, Phys. Rev. B 33 (1986) 8207.
[34] H. Wang, H.B. Wang, F.J. Yang, Y. Chen, C. Zhang, C.P. Yang, Q. Li, S.P. Wong, Nanotechnology 17 (2006) 4312.
[35] M.H. Huang, Y.Y. Wu, H.N. Feick, N. Tran, E. Weber, P.D. Yang, Adv. Mater. 13 (2001) 113.
[36] C. Li, G. Fang, Q. Fu, F. Su, G. Li, X.Z. Wu, X. Zhao, J. Cryst. Growth 292 (2006) 19.
[37] Y. Sun, N.G. Ndifor-Angwafor, D.J. Riley, M.N.R. Ashfold, Chem. Phys. Lett. 431 (2006) 352.
[38] T. Tatsumi, M. Fujita, N. Kavamoto, M. Sasajima, Y. Horikoshi, J. Appl. Phys. 43 (2004) 2602.
[39] X. Wei, B. Ban, C. Xue, C. Chen, M. Liu, J. Appl. Phys. 45 (2006) 8586.
[40] N.Y. Garces, L. Wang, L. Bai, N.C. Giles, L.E. Halliburton, G. Cantwell, Appl. Phys. Lett. 81 (2002) 622.
[41] T.G. Kryshtab, V.S. Khomchenko, V.P. Papusha, M.O. Mazin, Y.A. Tzykunov, Thin Solid Films 76 (2002) 403.
[42] Atul Gupta, Sunil Kumar, H.S. Bhatti, J. Mater. Sci.: Mater. Elect. 21 (2010) 765.
[43] R. Dingle, Phys. Rev. Lett. 23 (1969) 579.
[44] B. Lin, Z. Fu, Y. Jia, Appl. Phys. Lett. 79 (2001) 943.
[45] J.R. Smith, W.H. Vehse, Phys. Lett. 31A (1970) 147.
[46] V. Soriano, D. Galland, Phys. Stat. Sol. (b) 77 (1976) 739.
[47] D.M. Hofmann1, H. Zhou, D.R. Pfisterer, H. Alves, B.K. Meyer, P. Baranov, Phys. Stat. Sol. (c) 1 (2004) 908.
[48] J.A. Weil, J.R. Bolton, J.E. Wertz, Electron Paramagnetic Resonance-Elementary Theory and Practical Applications, Wiley, New York, 1994, 498.
[49] N.W. Aschcroft, N.D. Mermin, Solid State Physics, Harcourt College Publishers, New York, 2001, 656.